Open-boundary reflection of quantum well states at Pb(111)

M. Müller,[1] N. Néel,[1] S. Crampin,[2,*] and J. Kröger[1,†]
[1]*Institut für Physik, Technische Universität Ilmenau, D-98693 Ilmenau, Germany*
[2]*Department of Physics & Centre for Nanoscience and Nanotechnology, University of Bath, Bath BA2 7AY, United Kingdom*
(Received 4 August 2017; revised manuscript received 6 October 2017; published 20 November 2017)

Using a scanning tunneling microscope, confined electron states are studied that exist above subsurface nanometer-sized voids at Pb(111), where potential barriers at the parallel vacuum-Pb(111) and Pb(111)-void interfaces establish a principal series of quantum well states that are further confined laterally by strong reflection at the open boundaries at the edges of the void. The influence of the size, depth, and shape of the voids on the effectiveness of the lateral confinement is discussed. Standing wave patterns observed in differential conductance maps unravel the dispersion of the relevant underlying Pb electron states.

DOI: 10.1103/PhysRevB.96.205426

I. INTRODUCTION

Restricting the motion of electrons in metals or semiconductors to dimensions that are comparable to the Fermi wavelength λ_F is referred to as quantum confinement. The resulting quantization of electron states can alter the physical properties of the solid, in ways beneficial to a variety of applications including spintronics [1], quantum computing [2], optoelectronics [3,4], photovoltaics [5], and catalysis [6]. An important example of quantum confinement is within quantum wells formed in thin films and overlayers. While electrons in these systems are able to move freely in the plane of the film, the film-substrate and/or film-vacuum interfaces act as barriers, reflecting impinging electrons. At specific film thicknesses standing electron waves are established between the interfaces, giving rise to quantum well states (QWS). Since the first experimental evidence for QWS was reported, using the reflection of low-energy electrons from Au films deposited on Ir(111) [7], there has followed a wealth of experimental and theoretical work on QWS for a wide variety of film-substrate combinations [8], and the importance of QWS has been unraveled for, among others, monitoring film quality [9], chemical reactivity [10,11], crystal growth [12], magnetic interactions [13–15], oscillatory quantum size effects displayed by the surface energy and work function [16], and electron correlation effects such as thin-film superconductivity [17–19] and the Kondo effect [20,21].

QWS in thin films of the *sp* metal Pb in particular, and the associated physics, have been discussed in many reports, exemplified by the following: the presence of QWS was first noted in planar tunneling junction experiments, where Pb thin films served as one electrode deposited onto Al or Mg oxide barriers [22,23]. Helium atom scattering from Pb on Cu(111) unraveled the influence of quantum size effects on the growth mechanism [24], also seen in Pb(111) films deposited on highly oriented pyrolytic graphite [25]. Nanoscale Pb wedges on Si(111) showed clear evidence of electron interference fringes, a signature of electron confinement [26], and thin Pb films fabricated on Si(111) have been used to investigate the thin-film Hall effect [27] and conductivity [28], both exhibiting strong film-thickness variations and understood in terms of quantized electronic structure. Such thin films were further used for investigations into quasi-bilayer variations in atomic interlayer spacings [29] and for probing the step structure of buried metal/semiconductor interfaces in Pb on Si(111)-(6 × 6)Au [30]. QWS in Pb(111) films on Si, Cu, and Ag substrates have been used to gain a quantitative understanding of electron-phonon coupling in thin films and the lifetimes of confined electronic states [31–36].

Lateral electron confinement has likewise been observed, with real-space images of surface electron standing waves in the vicinity of noble-metal step edges [37–39] constituting seminal work that has seen artificially fabricated atom assemblies used as quantum corrals for electronic surface states [40–42] and nanometer-scaled clusters [43,44], vacancies [45,46], and molecular networks [47–50] shown to effectively confine electron motion. Laterally confined surface states have also been observed on narrow terraces [51] and vicinal surfaces [52–54], and recently electron confinement to graphene nanostructures has attracted considerable interest [55–60].

Further restriction of electron motion has been reported for atomic [61–66] and molecular [67,68] chains on surfaces, defects on semiconductor surfaces [69], colloidal semiconductor nanocrystals [70], and metal [71] and semiconductor [72] quantum dots, as well as for artificial atoms [73]. A beautiful demonstration of electron confinement is the observation of the quantum analog to whispering gallery modes in oligothiphene rings [74] and graphene [75].

The aforementioned examples reveal the panoply of confinement effects and highlight an important shared ingredient: for electron motion to be restricted to a specific region of space requires an effective potential well, enclosed by boundaries that reflect electron waves [76]. The confining potential wells may be provided by geometric constraints, such as boundaries of terraces and quantum corrals, atomic and molecular chain edges, and by the forbidden electron penetration into the vacuum or surface-projected energy gaps of the substrate.

We have recently reported a confinement mechanism affecting the conduction electrons of a metal [77], observed in the vicinity of nanometer-sized subsurface voids (or "cavities") at Pb(111). These cavities were engineered by Ar^+ ion bombardment and subsequent annealing, and are located several atomic layers beneath the Pb(111) surface. Similar

*s.crampin@bath.ac.uk
†joerg.kroeger@tu-ilmenau.de

 ©2017 American Physical Society

structures have previously been reported for Al(111) [78], Cu(100) [79–81], Cu(110) [80,82], Ag(100) [83], and Ag(111) [83] surfaces. These buried voids offer a unique opportunity to investigate both vertical and lateral confinement, with vertical confinement occurring in the thin Pb layer atop the void where the parallel void-Pb(111) and Pb(111)-vacuum interfaces lead to the formation of conventional QWS, and with additional reflection of electrons at the open boundaries where the thin Pb film above the void recovers its bulk thickness resulting in lateral confinement. The latter is noteworthy as it occurs despite the absence of a confining potential well in the lateral direction.

In the present article we expand upon our previous reported findings and unravel further aspects. We analyze real-space images measured above a buried void of electron standing wave patterns associated with the confinement, and use these to extract the dispersion of the underlying Pb states. Consideration of the Pb(111) thin film band structure allows us to understand how hybridization between Bragg-diffracted QWS results in distinctive aspects including band flattening and downward dispersing states that affect the observation of laterally confined states. We go beyond our previous analytical model [77] that assumed cylindrical cavities and infinite barrier potentials, presenting a scheme that allows us to model more realistic and varied void geometries, and finite potential barriers that allow charge spill-out. This approach is used to study the influence on the confinement of electrons of the size, shape, and depth beneath the substrate surface of the void.

II. EXPERIMENT

Experiments were performed with a scanning tunneling microscope (STM) operated in ultrahigh vacuum (10^{-9} Pa) and at low temperature (6 K). Atomically clean Pb(111) was obtained by repeated Ar^+ bombardment and annealing. To efficiently create subsurface voids the ion kinetic energy and current density at the sample were set to 1.1 keV and 5 μA/cm^2, respectively, with the ion beam impinging onto the surface at an angle of 30° with respect to the surface normal. Samples were subsequently annealed at 560 K for 20 min. All STM images were recorded at constant current with the bias voltage applied to the sample. Spectra of the differential conductance (dI/dV) were acquired at constant height by sinusoidally modulating the sample voltage (5 mV_{pp}, 6.3 kHz) and detecting the current response of the junction with a lock-in amplifier. For recording maps of dI/dV simultaneously with STM images a higher voltage modulation (20 mV_{pp}) was used.

III. MODELING

The electronic structure of thin Pb(111) films has been calculated within density functional theory, using the plane wave pseudopotential code CASTEP [84]. *Ab initio* energy bands for film thickness between 2 and 14 layers have been calculated using both the local-density approximation and the general-gradient approximation to the exchange functional, default "on-the-fly" ultrasoft pseudopotentials, 240 eV plane wave basis cutoff energy, $41 \times 41 \times 1$ Monkhorst-Pack k-point grids, and a 15 Å vacuum gap. Geometry optimization minimized forces to <0.05 eV/Å.

The *ab initio* energy bands provide a reference set of film-thickness-dependent QWS energies, which through comparison with experiment enable identification of the depth of subsurface voids (Sec. IV A). We also make a direct comparison between the dispersion of the Pb(111) states extracted from the standing wave patterns of laterally confined electrons above nanocavities and the *ab initio* band structure (Sec. IV C). Analysis of these energy bands also justifies the use of a simpler free-electron model to describe the lateral confinement of states atop finite-sized voids. To elucidate the nature of these states a simplified model is considered in which electrons move in an effective potential $V(\boldsymbol{r})$. This consists of a planar potential $V_{\rm jel}(z)$ describing the surface barriers, and which is taken from a self-consistent stabilized jellium [85] calculation for a 6-layer film, and to which a pseudopotential

$$V_{\rm ps}(\boldsymbol{r}) = \sum_{\boldsymbol{G}} V_{\boldsymbol{G}} e^{i\boldsymbol{G}\cdot(\boldsymbol{r}-\boldsymbol{r}_0)}\theta(3d_{111} - |z|) \qquad (1)$$

is added. The Heaviside step function θ ensures that the pseudopotential only acts over the atomic planes of the film (layer-layer spacing $d_{111} = a/\sqrt{3}$), $\boldsymbol{r}_0$ is the location of a surface atom, and since the aim here is merely interpretive we restrict the sum to the set of smallest nonvanishing reciprocal-lattice vectors, of magnitude $|\boldsymbol{G}| = \sqrt{3}(2\pi/a)$, which provide the dominant contribution to the ion core pseudopotential acting on states near the Fermi level [86]. Two of the reciprocal-lattice vectors are parallel to the surface normal $\hat{\mathbf{z}}$, so that the film potential can be written $V(\boldsymbol{r}) = V(z) + \Delta V(\boldsymbol{r})$ with planar potential

$$V(z) = V_{\rm jel}(z) + 2V_{111}\cos[G(z - z_0)]\Theta(3d_{111} - |z|) \qquad (2)$$

and corrugation

$$\Delta V(\boldsymbol{r}) = V_{111} \sum_{\boldsymbol{G}}{}' e^{i\boldsymbol{G}\cdot(\boldsymbol{r}-\boldsymbol{r}_0)}\Theta(3d_{111} - |z|); \qquad (3)$$

the prime denoting the summation is over the remaining 6 terms. We use $V_{111} = -1.142$ eV for the coefficient, as determined by previous fitting of Fermi surface data [86].

Figure 1(a) shows the thin-film energy bands when the potential consists of just the planar component $V(z)$, calculated for wave vectors along the path 2M-Γ-2K, where high-symmetry points $\mathrm{M} = (0, \sqrt{2/3})(2\pi/a)$ and $\mathrm{K} = (\sqrt{8}/3, 0)(2\pi/a)$ in the geometry used [right panel of Fig. 1(a)]. Translational invariance means free-electron behavior in the plane of the film and all bands disperse identically with free-electron effective mass. Including the corrugation ΔV but scaled to infinitesimal strength changes the translational symmetry of the surface, modifying the band structure [Fig. 1(b)]. Replica bands appear, centered on each of the surface reciprocal lattice points, corresponding to diffracted free-electron (in-plane) states. Finally, energy bands calculated using the full corrugation potential ΔV are shown in Fig. 1(c), and exhibit further changes. Hybridization between states now creates a gap in the spectrum below −4 eV, and for higher lying states creates some complex dispersions where bands previously crossed. Figure 1(c) highlights these effects on the QWS around the Fermi energy ($\varepsilon_{\rm F}$). For wave vectors close to Γ the occupied QWS continue to show free-electron-like dispersion, but the unoccupied QWS are noticeably flattened, indicating an increase in effective mass, an effect

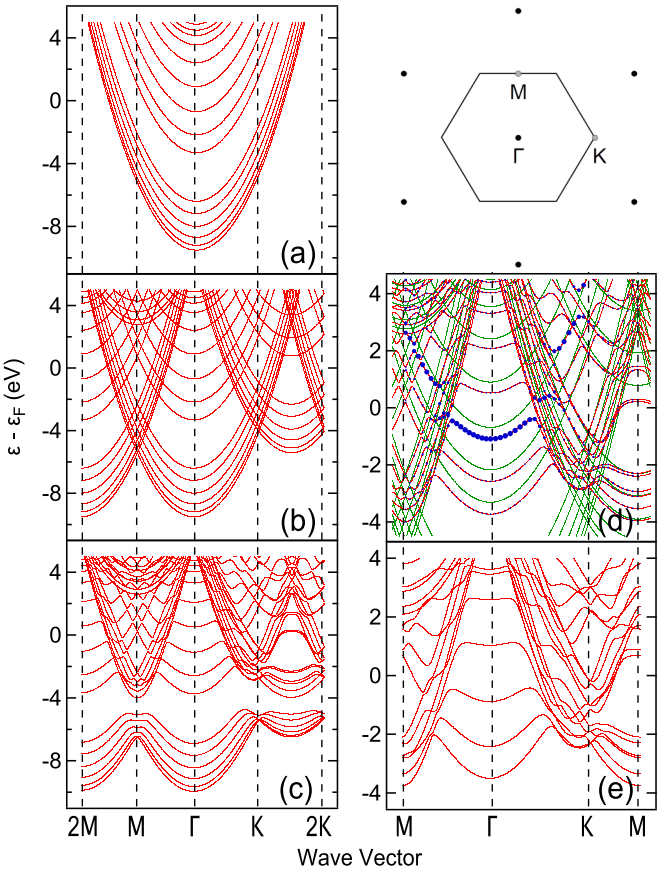

FIG. 1. 6-layer Pb(111) thin film energy bands. (a)–(d) Model and (e) *ab initio* calculations. (a) QWS energy bands obtained using the planar-averaged potential only, showing free-electron dispersion. Right: Surface Brillouin zone with high-symmetry points shown. (b) Energy bands obtained including the corrugation potential scaled to infinitesimal strength, changing the translational symmetry of the surface. (c) Energy bands obtained using the full ionic pseudopotential, showing hybridization between bands centered on different surface reciprocal lattice vectors. (d) Direct comparison of unhybridized (green, ΔV infinitesimal) and hybridized (red, ΔV unscaled) energy bands near the Fermi energy (ε_F). The area of the blue filled circles illustrates the relative orbital overlap of the corresponding state with the highest occupied quantum well state at Γ. (e) *Ab initio* energy bands for a 6-layer Pb(111) film.

that becomes more significant as one moves up the ladder of QWS. Furthermore, both occupied and unoccupied QWS only disperse upwards over a finite range of energies, before turning downwards and then dispersing as the unhybridized bands centered on neighboring reciprocal lattice points. This results in especially narrow bandwidths of free-electron behavior for the unoccupied QWS.

The associated wave functions have Bloch form $\psi_{n,\boldsymbol{k}}(\boldsymbol{r}) = u_{n,\boldsymbol{k}}(\boldsymbol{r})e^{i\boldsymbol{k}\cdot\boldsymbol{r}}$ with band index n and wave vector $\boldsymbol{k}$. To illustrate the variation in the wave function of the QWS we calculate the overlap $|\langle u_{n,\boldsymbol{k}}|u_{\mathrm{HOQWS},\Gamma}\rangle|^2$ for each state $(n,\boldsymbol{k})$, with HOQWS indicating the highest occupied QWS, and display this through the area of blue disks overlaying the energy bands in Fig. 1(d). At Γ the overlap vanishes for all states other than the HOQWS. Away from Γ, the states within the HOQWS band remain largely unchanged throughout the quadratically dispersing portion of the band, while other states at similar energies are essentially orthogonal. As a consequence, in the presence of slowly varying perturbations the states within this portion of the HOQWS will be largely uncoupled from the rest of the thin-film states, and this permits a simpler description of such states in terms of purely free-electron-like (in-plane) states corresponding to those of a planar potential. Finally, we note that the remarkable similarity between model [Fig. 1(d)] and *ab initio* [Fig. 1(e)] energy bands indicates that the insights obtained from this model are applicable to real Pb films. Similar behavior is seen for other film thicknesses, as previously reported [25,87–90].

Building upon these observations, in Ref. [77] confinement via open-boundary scattering was modeled using an idealized model, treating Pb as a free-electron metal and with voids described as cylindrically symmetric volumes from which electrons were fully excluded, with radius S and extending from a depth D beneath the surface. The Pb(111) surface barrier was similarly modeled by an infinite step potential. Here we supplement that model, which permitted an analytic analysis, with numerical results obtained for a more general description in which the void and surface barrier are described by finite potential barriers and with more varied void geometries. The former enables charge to more realistically spill-out of the surface and penetrate into the void. In the region outside both the surface barrier (assumed planar and occupying $z < 0$) and the nanovoid we continue to assume free-electron propagation so that the model remains primarily restricted to the free-electron-like portion of the occupied QWS. The electronic structure is determined from the single-particle Green's function $G(\boldsymbol{r},\boldsymbol{r}';\varepsilon)$ satisfying $(\mathcal{H}-\varepsilon)G = -\delta(\boldsymbol{r}-\boldsymbol{r}')$, which for $z < z'$ has the form (energy dependence suppressed)

$$G(\boldsymbol{r},\boldsymbol{r}') = \sum_{MM'}\int dk \int dk' \Psi^{<}_{Mk}(\boldsymbol{r})\,\mathcal{G}_{MM'}(k,k') \times \Psi^{>}_{M'k'}(\boldsymbol{r}')/(i\kappa'), \tag{4}$$

where in the region of constant potential between the surface barrier and void potential, the wave functions $\Psi^{>}$ and $\Psi^{<}$ are

$$\Psi^{<}_{Mk}(\boldsymbol{r}) = \chi^{-}_{Mk}(\boldsymbol{r}) + \chi^{+}_{Mk}(\boldsymbol{r})\,\mathcal{L}(k),$$

$$\Psi^{>}_{Mk}(\boldsymbol{r}) = \chi^{+\times}_{Mk}(\boldsymbol{r}) + \sum_{M'}\int dk'\,\mathcal{R}_{MM'}(k,k')\chi^{-\times}_{M'k'}(\boldsymbol{r}), \tag{5}$$

corresponding to combinations of forward (+) and backward (−) traveling cylindrical waves,

$$\chi^{\pm}_{Mk}(\boldsymbol{r}) = \chi_{Mk}(\boldsymbol{R})e^{\pm i\kappa z}, \quad \chi_{Mk}(\boldsymbol{R}) = \sqrt{k/2\pi}\,J_M(kR)e^{iM\varphi}, \tag{6}$$

where $\boldsymbol{r} = (R,\varphi,z)$, $\boldsymbol{R} = (R,\varphi)$, k is the wave number in the plane perpendicular to $\hat{\boldsymbol{z}}$, J_M is a cylindrical Bessel function, angular momentum quantum number $M \in \mathbb{Z}$, $\kappa = \sqrt{2\varepsilon - k^2}$, and in Eq. (5) $\times$ denotes conjugation of the angular factor only. The void is assumed to be centered laterally at $R = 0$. $\mathcal{L}$ and $\mathcal{R}$ are barrier and void reflection coefficients, respectively, with $\mathcal{L}$ in general found by numerical integration of the

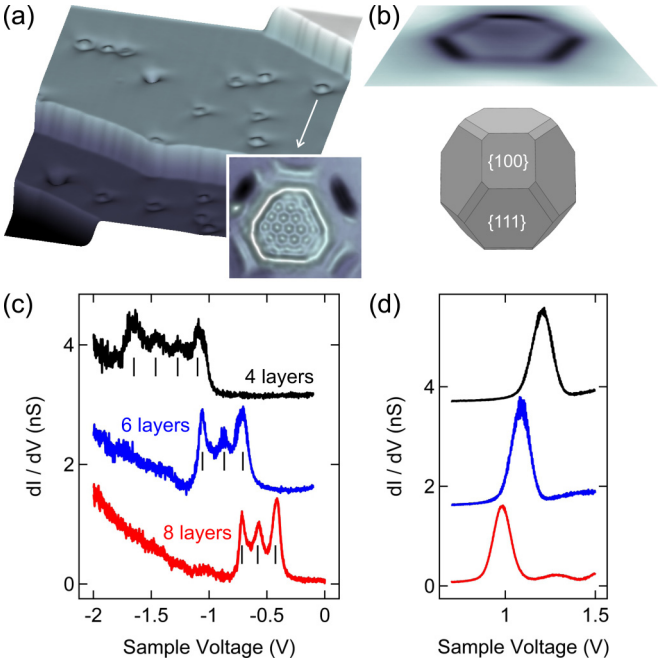

FIG. 2. (a) Pseudo-three-dimensional STM image of Pb(111) revealing cavities buried beneath two terraces (0.5 nA, 1.2 V, 1000 Å × 1000 Å). Inset: Constant-current map of dI/dV recorded atop the indicated cavity showing electron standing wave patterns (1 nA, 0.4 V, 78 Å × 78 Å). (b) Schematic illustration of a subsurface nanocavity, with geometry based on the Wulff construction using (111), (110), and (100) Pb surface energies. {111} and {100} facets are indicated; {110} facets appear as the smallest regions of the Wulff construction. (c) Spectra of dI/dV acquired atop the center of cavities with similar radii of ≈20 Å residing at the indicated depths, and showing the signature of the HOQWS. The spectra for 6 and 4 layers have been vertically offset by 1.5 nS and 3 nS, respectively. The vertical bars indicate the spectroscopic fine structure due to lateral confinement. Prior to data acquisition the feedback loop had been disabled at 1 nA, −2 V for all spectra. (d) As (c), showing the spectroscopic signatures of the LUQWS. The spectra for 6 and 4 layers are vertically offset by 1.6 nS and 3.7 nS, respectively. The feedback loop had been disabled at 0.5 nA, 2.3 V prior to data acquisition.

one-dimensional Schrödinger equation: for a step barrier, height w at $z = 0$, $\mathcal{L} = (i\kappa - \gamma)/(i\kappa + \gamma)$ with $\gamma = \sqrt{2(w - \varepsilon) + k^2}$. The void reflection coefficient $\mathcal{R}$ is calculated using the method outlined in the Appendix. In Eq. (4) $\mathcal{G}$ is obtained from the integral equation expressed formally as $\mathcal{G} = 1 + \mathcal{R}\,\mathcal{L}\,\mathcal{G}$.

IV. RESULTS AND DISCUSSION

A. Geometric and electronic properties of buried cavities

Figure 2(a) shows the pseudo-three-dimensional STM image of a freshly prepared Pb(111) surface. Buried cavities reveal themselves as depressions or protrusions with an irregular hexagonal circumference, and apparent diameters that range between 25 and 70 Å. Their geometric structure reflects the minimized interfacial free energy according to the Wulff construction [Fig. 2(b)]. The upper {100} and {111} side facets of the cavity scatter electrons and give rise to interference effects, with the characteristic fringes visible both in Fig. 2(b) and outside the central confinement pattern present in the inset to Fig. 2(a) similar to those previously observed and reported for subsurface cavities at Cu(110) [82].

The parallel Pb(111) surface and upper face of the void form an electron resonator that quantizes the electron states according to their variation in the direction normal to the surface. The energies of these QWS depend strongly on the Pb layer thickness, so that the location and spacing of the HOQWS [Fig. 2(c)] and lowest unoccupied QWS (LUQWS) [Fig. 2(d)] of these states provide a signature of the depth of the void. This depth is identified by comparison with the calculated *ab initio* thin-film energy bands. The most abundant Pb film thicknesses deduced above the buried voids are 4, 6, and 8 atomic layers, indicating a preference for even numbers of Pb atomic layers and an electronic stabilization effect influencing the void depth. Indeed, the Fermi wavelength of Pb electron states propagating perpendicular to the (111) surface is approximately four times the (111) layer-layer spacing and therefore a bilayer periodicity of the density of states at ε_F may be expected. Bilayer periodicity in other Pb thin film properties have likewise been reported, including the superconducting transition temperature in ultrathin Pb films [17–19], surface phonon frequencies [89], preferred island heights [91,92], and the work function [93,94].

The dI/dV spectra acquired atop the center of nearly equally sized ($S \approx 20$ Å) cavities at different depths [Fig. 2(c)] show that the bias voltage range covered by the feature associated with the HOQWS decreases from ≈0.7 V (4 layers) via ≈0.45 V (6 layers) to ≈0.35 V (8 layers) as the feature moves to zero bias voltage with increasing Pb film thickness. This is consistent with the behavior of the free-electron-like portion of the HOQWS seen in the thin-film energy bands [Figs. 1(d), 1(e)], which as noted in Sec. III have a finite extent due to hybridization with Bragg-diffracted states. The higher in energy the QWS lies, the smaller the range of wave vectors before the dispersing band is significantly affected by this hybridization and loses its character. Concomitantly the bandwidth decreases with increasing QWS energy, as seen in Fig. 2(c). The hybridization affects the higher-lying LUQWS even more, and hence explains the broader appearance of the HOQWS than the LUQWS [Fig. 2(d)] for a given film thickness [36]. Characteristic spectroscopic fine structure is clearly visible within the bandwidth of the HOQWS, indicated by vertical bars in Fig. 2(c). These arise from lateral confinement of the QWS electrons to the region atop the cavity [77] and are discussed in the following section. It is noteworthy that spectra such as those in Fig. 2(c) recorded at temperatures above and below the critical temperature of Pb ($T_c = 7.2$ K) show no significant differences, confirming that the superconducting state of Pb is not relevant to these findings.

The inset to Fig. 2(a) displays a constant-current dI/dV map recorded above the indicated cavity, revealing rich structure with a regular hexagonal pattern visible in the central area. The size ($\gtrsim$7 Å) and voltage dependence of the pattern points to an electronic origin, which we attribute to the quantum interference pattern resulting also from reflection of QWS electrons at the open boundary where the thin Pb film between the cavity and the Pb(111) surface recovers its

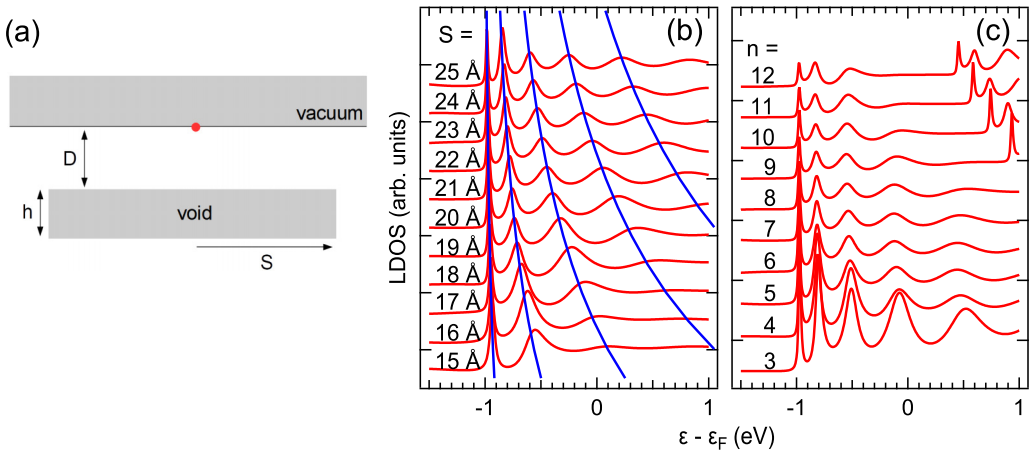

FIG. 3. Lateral confinement. (a) Model geometry. A cylindrically symmetric void of radius S, thickness h is positioned a depth D beneath the surface. Gray regions correspond to potential v. The red dot indicates the position at which the LDOS is evaluated. (b) Calculated LDOS atop voids (height $h = 8$ Å, depth $D = 11.4$ Å, potential $v = 13.6$ eV). Results obtained for different radii S are offset vertically (red). Also shown (blue) are the expected peak positions assuming ideal reflection at the void edge (see text). (c) Calculated LDOS above voids (cylindrical volume, $h = 8$ Å, $S = 23$ Å, $v = 13.6$ eV) at various depths. Each spectrum (vertically offset) is calculated with the void at a depth placing the onset of the nth-lowest QWS at energy $E_n = \varepsilon_F - 1.0$ eV.

bulk thickness. Analysis of these patterns is used to extract the dispersion of the underlying electron bands (see below).

B. Lateral confinement

We have previously [77] recognized the fine structure present in dI/dV spectra recorded atop subsurface voids as resulting from further lateral confinement of the principally vertically confined QWS electrons, due to open-boundary reflection at the edges of the void. Here, the nature of this confinement is further explored through calculation using the approach described in Sec. III. First, we investigate how the size and depth of the void impact the spectroscopic fine structure induced by the lateral confinement. Second, more varied void geometries are considered. Throughout, the calculations reported here treat the vacuum-Pb and Pb-void barriers as finite step potentials, rather than the infinite barriers used previously [77].

We place the surface barrier at $z = 0$ and consider the void as presenting a face a distance D from the surface [Fig. 3(a)]. The local density of states (LDOS) is obtained from the Green's function calculated as described in Sec. III as $n(\boldsymbol{r};\varepsilon) = -(1/\pi)\mathrm{Im}G(\boldsymbol{r},\boldsymbol{r};\varepsilon)$. Figure 3(b) shows $n(\boldsymbol{r} = 0,\varepsilon)$ atop cylindrically shaped voids of varying radii S, fixed thickness $h = 8$ Å, located at a constant depth $D = 11.4$ Å. Increasing the thickness has no effect on the results. A void potential of strength $v = 13.6$ eV and $\varepsilon_F = 9.47$ eV for Pb is used giving rise to the HOQWS, the sixth-lowest QWS at this depth, at threshold energy $E_6 = \varepsilon_F - 1.0$ eV. For $S = \infty$, corresponding to an infinitely extended thin film, the LDOS associated with the QWS takes on the appearance of a steplike increase at energy E_6 (not shown), broadened slightly by the 5 meV imaginary energy included in calculations for numerical purposes. Unlike the experimental spectra of Fig. 2(c) there is no upper band edge. This is because our calculations consider only free-electron-like dispersion, and omit hybridization effects between different QWS bands discussed in Sec. III, that create an upper limit to the HOQWS band. As evident in Fig. 3(b), atop voids of finite radius the LDOS within the QWS subband instead takes on the appearance of a series of resonant peaks, with the jth peak occurring at

$$\varepsilon_j = E_6 + \frac{\hbar^2}{2m}\left(\frac{\alpha_{j,0}}{S}\right)^2, \tag{7}$$

where $\alpha_{j,0}$ (=2.405, 5.520, 8.654, . . . for $j = 1,2,3,\ldots$) is the jth zero of the Bessel function J_0. The blue curves in Fig. 3(b) trace out the relationship of Eq. (7). The origin of this behavior lies in strong reflection of laterally outward traveling free-electron-like states present in the region above the void, at the radius S where the opening up of the full depth of the Pb crystal acts like a hard-wall boundary. This has the effect of imposing a node in the radial wave function $J_M(kR)$ at $R = S$, quantizing the wave number k. Only states with $M = 0$ additionally have nonvanishing amplitude at $R = 0$, and so contribute to the LDOS at $\boldsymbol{r} = 0$, and hence the existence of quantized energies given by Eq. (7). Spectra calculated above voids with hexagonal cross section are very similar but have peaks at energies given by Eq. (7) with $\alpha_{j,0} \to \alpha_{j,\mathrm{A1}}$ where $\alpha_{j,\mathrm{A1}} = 2.317, 5.303, 8.218, \ldots$ for $j = 1,2,3,\ldots$. These are the eigenvalues of A1-symmetry states confined within a hexagon of inscribed circular radius S [95]. The lower symmetry of the hexagonal system mixes cylindrical states [Eq. (6)] with different angular momenta and makes calculations significantly more expensive. Hence in the following we focus on the cylindrical case.

The levels are resonances due to the lossy character of the boundary reflection, with the variation in the peak widths due to the combined effects of the energy dependence of the losses and the increasing boundary collision rate with energy [77]. This makes clear why no spectroscopic fine structure associated with laterally confined states is seen in the LUQWS band, Fig. 2(d). Hybridization between the individual QWS (Sec. III) causes the LUQWS to have a narrower bandwidth and greater effective mass than the HOQWS, the latter [through

Eq. (7)] meaning the states are more closely spaced than in the HOQWS. This spacing is less than the resonance widths, which also in the experimental spectra include contributions from electron-electron and electron-phonon scattering [77], to the extent that they cannot be resolved.

Next, the effect of the depth of the void is unveiled. To do this, we exploit the continuum nature of our model to position voids at a succession of depths D_n that each place the nth QWS at the same threshold energy $\varepsilon_F - 1.0$ eV (e.g., $D_n = 9.3$ Å, 11.4 Å, 13.5 Å for $n = 5, 6, 7$). The corresponding spectra are shown in Fig. 3(c). The radius and thickness of the cylindrical void are held fixed, with $S = 23$ Å and $h = 8$ Å, respectively. The energy spacing of the principal series of QWS associated with confinement normal to the surface decreases with increasing void depth, such that the spectra calculated for depth D_9 and above also show the LUQWS in the energy range displayed.

It can be seen from Fig. 3(c) that the location of spectral features within the QWS subband are not sensitive to the depth of the void. This is consistent with their origin being energy quantization associated with electron confinement caused by open-boundary reflection at the edge radius, which is unchanging. However, the width of the resonances that make up the spectra do change, becoming broader with increasing void depth, such that whereas the first 5 peaks are clearly resolvable for the depth D_3, this drops to only 3 for D_{12} (=24.1 Å). Therefore, the effects of lateral confinement are visible above voids whose depth is comparable to the void radius, but the effectiveness of the confinement decreases with void depth, due to an increase in the lossy character of the elastic boundary scattering [46,96,97]. One consequence of this is that the use of subsurface voids to induce spectral structure from which intrinsic electron-electron and electron-phonon scattering rates can be deduced [77] will be limited to shallower voids, else elastic scattering effects will dominate linewidths and prevent the smaller intrinsic lifetime effects from being extracted.

The calculations nicely reproduce spectroscopic data obtained from buried voids. Figures 4(a) and 4(b) compare experimental [Fig. 4(a)] and calculated [Fig. 4(b)] data for voids with similar radii $S = 20 \pm 2$ Å and buried 4, 6, 8 layers beneath the Pb(111) surface. All spectra show the HOQWS whose covered bias voltage and calculated energy ranges have been shifted by the QWS onset voltage and energy to facilitate the comparison. The additional feature in the experimental 4-layer dI/dV spectrum slightly below 0.5 V [Fig. 4(a), top] is absent from the calculated LDOS. As previously shown [77], such additional low-amplitude peaks are consistent with expected contributions from lower-symmetry states at slightly off-center locations above voids in the spectroscopy experiments. Another difference between the calculated and measured spectra is the more uniform spacing of the peaks measured above 6-layer and 8-layer deep voids. This is due to the hybridization effects not included in the calculations and responsible for the measured spectrum having an upper band edge, and which also lower in energy the upper parts of the QWS band. This causes a downward shift in the third laterally quantized state, creating more uniform spacings. A similarly good agreement between experiment and theory is achieved for 4-layer deep voids with different radii [Figs. 4(c), 4(d)].

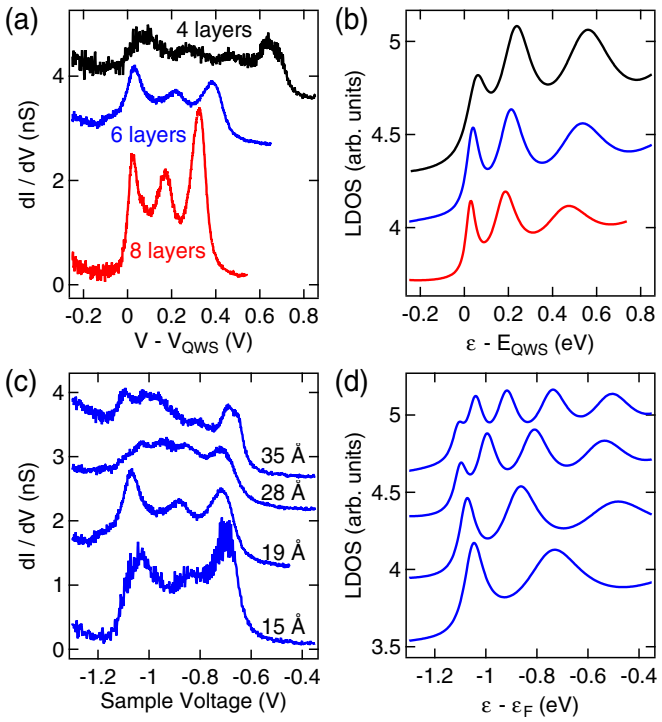

FIG. 4. Voids of similar size at different depths, and with different radii at the same depth. (a) dI/dV spectra acquired atop the center of voids with radii ≈20 Å and indicated depths. The bias voltage (V) of each spectrum was adjusted in order to align the onset of the QWS ($V_{QWS} = 1.73$ V, 1.10 V, 0.74 V for 4, 6, 8 layers, respectively). The dI/dV data for 4 (6) layers are vertically offset by 3.4 nS (2.5 nS). The feedback loop was disabled at 1 nA, −2 V (4 layers), −1.75 V (6 layers), −1.2 V (8 layers). (b) Calculated LDOS for cylindrical cavity ($h = 8$ Å, $S = 21$ Å) 4 (top), 6 (middle), 8 (bottom) layers beneath the Pb(111) surface. The energy axis was adjusted to align the QWS onsets. The top and middle spectra are vertically offset for clarity. (c) dI/dV spectra acquired atop the center of voids buried 6 layers beneath the Pb(111) surface and with indicated radii. The spectra are vertically offset by 1.2 nS (19 Å), 2 nS (28 Å), 2.6 nS (35 Å). Feedback loop parameters: 1 nA, −1.5 V (15 Å, 28 Å, 35 Å), −1.75 V (19 Å). (d) Calculated LDOS for cylindrical cavity ($h =$ 8 Å) with radii (from bottom to top) 15 Å, 19 Å, 28 Å, 35 Å and 6 layers beneath the Pb(111) surface. Data are vertically offset for clarity.

As a next step more realistic void geometries than the hitherto assumed cylindrical shape are considered in the calculations. The actual voids in face-centered cubic (fcc) Pb have a polyhedral shape, with sloping edges, whereas the cylindrical model presents an abrupt transition in Pb thickness at radius S. To understand the effect of a more gradual transition, we have also calculated the LDOS atop cylindrically symmetric voids whose radius increases from 15 Å on the upper face to 23 Å, with the angle of side slope varying between $\theta = 0°$ and 45° [Fig. 5(a)]. $\theta = 0°$ is equivalent to a cylinder of radius 23 Å, while for $\theta = 45°$ the full width of 23 Å is reached at a depth 8 Å beneath the upper face. Figure 5(b) shows the resulting LDOS at $\boldsymbol{r} = 0$ above the center of the void. For the very shallowest of slopes ($\theta \lesssim 1°$) the spectrum consists of 5 resonant levels, similar to that

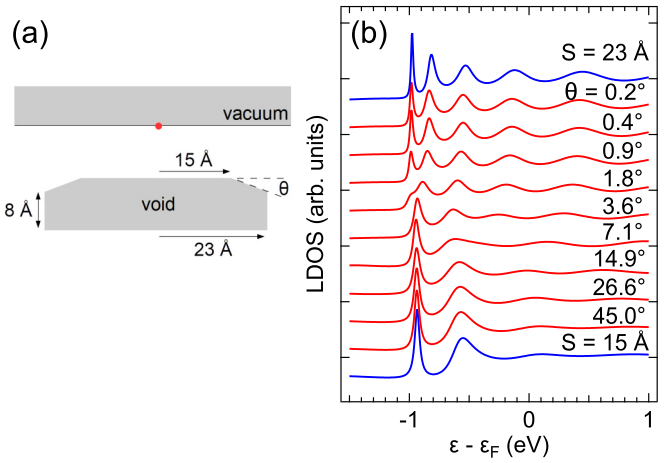

FIG. 5. Effect of void profile. (a) Model geometry. The radius of the cylindrically symmetric void increases from 15 Å to 23 Å at a slope angle θ, with base thickness of 8 Å. Shaded regions correspond to potential v. The red circle indicates the position at which the LDOS is evaluated. (b) Calculated LDOS atop the center of cylindrical voids with sloping edges, at depth $D = 11.4$ Å. Spectra calculated with different slope angles θ (red) are offset for clarity. Also shown for reference are the calculated spectra atop voids of uniform radii $S =$ 15 Å and $S = 23$ Å (blue), at depth $D = 11.4$ Å.

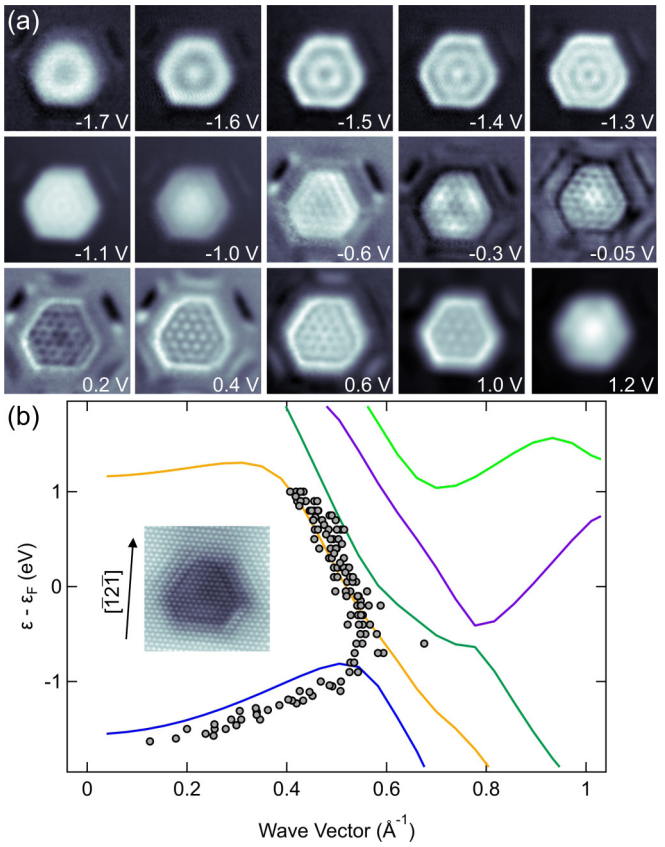

FIG. 6. Dispersion of QWS. (a) Gallery of constant-current dI/dV maps recorded atop a cavity buried 4 atomic layers beneath the Pb(111) surface at the indicated voltages (1 nA, 78 Å × 78 Å). (b) Experimental (dots) and calculated (lines) QWS band dispersion. Experimentally, the wave vector was extracted from the relevant periodicities visible in the dI/dV maps of six different cavities. The calculations were performed for a 4-layer Pb(111) thin film. The wave vector is oriented along the Γ M direction of the surface Brillouin zone, corresponding to the $\langle\bar{1}2\bar{1}\rangle$ crystallographic direction of Pb(111). Inset: Atomically resolved STM image of the surface region atop a buried cavity with indicated direction (0.5 nA, 0.3 V, 78 Å × 78 Å).

associated with an ideal cylinder of radius $S = 23$ Å, but it then evolves rapidly over a narrow range of slopes (angles $1^\circ \lesssim \theta \lesssim 7^\circ$), after which for slopes with $\theta \approx 14^\circ$ and above the spectrum consists of 3 peaks and has the appearance of that found above an ideal cylinder with radius $S = 15$ Å, there being very little difference in the position and width of the lowest resonances. These results indicate that sloping edges inclined at angles above $\theta \approx 14^\circ$ reflect electrons similarly to abrupt edges, especially within ~0.5 eV of the band edge. The polyhedral voids within the fcc Pb crystal, Fig. 2(b), have facets that slope at angles of 54.7° ({111}, {100}) and 35.3° ({110}), and so fall within this category. Lateral confinement is to the area above the upper hexagonal face of the polyhedral void.

C. Quantum well state dispersion

Figure 6(a) presents a collection of voltage-dependent constant-current dI/dV maps measured above a 4-layer deep void. The voltage range spans the HOQWS [onset ≈ − 1.7 V, Fig. 2(c)] and the LUQWS [onset ≈1.1 V, Fig. 2(d)]. From −1.7 V to −1.1 V the central interference pattern resembles a set of concentric rings, whose number increases with increasing voltage. Around −1.0 V the pattern is rather featureless. For bias voltages $\geqslant -0.6$ V the standing wave pattern suddenly takes on a more complex appearance, presenting a hexagonal arrangement of antinodes whose pitch *decreases* with increasing voltage. These observations are indicative of two different electron bands—one dispersing upward, the other downward—being involved in the standing wave patterns.

For the extraction of dispersion relations the raw constant-current dI/dV data [Fig. 6(a)] were normalized in order to compensate for the inevitable tip displacement during data acquisition [98]. The transformed data sets represent a better approximation to the LDOS [98] and serve as a more accurate source for the dispersion curves [99]. Mutual distances between nodes and antinodes of the resulting electron standing wave patterns were then determined along $\langle\bar{1}2\bar{1}\rangle$ [inset to Fig. 6(b)], which corresponds to the Γ M direction in reciprocal space [Fig. 1(a)]. These distances were identified with $\lambda/2$, where λ is the electron wavelength. Indeed, an electron wave with incident wave vector k is reflected into a state $-k$ giving rise to a standing wave with $2k$. Therefore, by analyzing standing wave patterns, dispersion relations with wave vectors throughout the surface Brillouin zone may be probed. Figure 6(b) shows the resulting experimentally extracted dispersion (dots) where $\varepsilon - \varepsilon_F = eV$ (e: elementary charge) is plotted versus the wave vector $2\pi/\lambda$. The full lines in Fig. 6(b) present the calculated band structure of a 4-layer thick Pb(111) thin film along Γ M. The HOQWS (LUQWS) dispersion is shown by a blue (orange) line. The HOQWS exhibits a nearly free-electron dispersion for small

wave vectors (<0.5 Å^{-1}) but beyond this it first flattens, and then disperses downwards, with an upper band edge at around -0.8 eV. Above this, the states within the Pb thin film are derived from downward-dispersing Bragg-diffracted bands. This explains the crossover in behavior exhibited in the dI/dV maps Fig. 6(a). Below ≈ -0.8 eV the maps are associated with free-electron-like states whose behavior is similar to that described by our earlier model. They are confined by reflection at the hexagonal edges of the upper face of the polyhedral voids, which act as a hard-wall potential. Hence the close similarity in the appearance of the maps with those observed above hexagonal islands on Ag(111) [43], which also have an interpretation in terms of confined free-electron-like states, in that case Shockley surface states confined by the rapid rise in the potential at the geometrical edges of the islands.

Maps of dI/dV around ≈ -1 V [Fig. 6(a)] do not show clearly resolved interference patterns, due to the rather flat energy band at that energy, meaning electron states with various wave vectors and similar energies will contribute to the interference pattern, resulting in a smeared dI/dV map. Above -0.6 V the responsible electronic states suddenly derive from a different energy band, hence the sudden change in complexity, of the dI/dV maps, and the rather steep downward dispersion of the band accounts for the decreasing pitch of the antinodes for increasing voltage. The states associated with this band have very different character to the free-electron-like states of the HOQWS, but evidently also experience reflection at the open boundary at the void edge, manifested by the resulting interference pattern. Finally, at 1.2 V the pattern becomes smeared out again as the voltage coincides with the flat portion of the LUQWS band.

V. SUMMARY

We have presented results from a study of the confined electron states present above subsurface nanometer-sized voids at Pb(111), formed by Ar^+ bombardment and annealing. In the Pb above the void, the parallel vacuum-Pb(111) and Pb(111)-void interfaces form a resonator system establishing a principal series of QWS that we study using an STM. Electrons in the QWS are also confined laterally by strong reflection at the open boundaries at the edges of the void, giving rise to fine structure in dI/dV spectra. Modeling shows that the lateral confinement is most effective for larger, shallower voids, and that the sloping edges of the polyhedral voids act as abrupt edges. Maps of dI/dV recorded above buried voids reveal detailed interference patterns, with a sudden change in complexity understood in terms of the dispersion of the underlying Pb thin film states.

ACKNOWLEDGMENTS

Financial support by the Carl Zeiss Foundation and the Deutsche Forschungsgemeinschaft through KR 2912/10-1 is acknowledged. This research made use of the Balena High Performance Computing (HPC) Service at the University of Bath.

APPENDIX: VOID REFLECTIVITY

We calculate the reflectivity $\mathcal{R}$ of the void potential by dividing it into n slices of thickness d, and determining the total reflectivity from the scattering properties of the individual slices. Slice j corresponds to the region with $|z - z_j| < d/2$, and in isolation scatters incident forward (+) or backward (−) traveling cylindrical waves as

$$\Psi^{+}_{Mk}(\boldsymbol{r}) = \begin{cases} \chi^{+}_{Mk}(\boldsymbol{r}_j) + \sum_{M'} \int dk' \chi^{-}_{M'k'}(\boldsymbol{r}_j) r^{-+}_{j,M'M}(k',k), & z < z_j - d/2, \\ \sum_{M'} \int dk' \chi^{+}_{M'k'}(\boldsymbol{r}_j) t^{++}_{j,M'M}(k',k), & z > z_j + d/2, \end{cases}$$

$$\Psi^{-}_{Mk}(\boldsymbol{r}) = \begin{cases} \chi^{-}_{Mk}(\boldsymbol{r}_j) + \sum_{M'} \int dk' \chi^{+}_{M'k'}(\boldsymbol{r}_j) r^{+-}_{j,M'M}(k',k), & z > z_j + d/2, \\ \sum_{M'} \int dk' \chi^{-}_{M'k'}(\boldsymbol{r}_j) t^{--}_{j,M'M}(k',k), & z < z_j - d/2, \end{cases} \tag{A1}$$

where $\boldsymbol{r}_j = \boldsymbol{r} - z_j \hat{\boldsymbol{z}}$. The reflectivity is found by recursively applying for $j = n-1, \ldots, 1$

$$r^{-+}_{j,n} = r^{-+}_{j} + t^{--}_{j} p^{-}_{j+1} r^{-+}_{j+1,n} p^{+}_{j} (1 - r^{+-}_{j} p^{-}_{j+1} r^{-+}_{j+1,n} p^{+}_{j})^{-1} t^{++}_{j}, \tag{A2}$$

which gives the reflectivity of the combined region comprising slabs j through n, $r^{-+}_{j,n}$, in terms of the scattering properties of slice j and the reflectivity $r^{-+}_{j+1,n}$. The void reflectivity is $\mathcal{R} = r^{-+}_{1,n}$. Use of Eq. (A2) starts with $r^{-+}_{n,n} = r^{+-}_{n}$, multiplication corresponds to, e.g.,

$$a\, b \to \sum_{M'} \int dk' a_{MM'}(k,k') b_{M'M''}(k',k''), \tag{A3}$$

and the propagator $p^{\pm}_{j} = e^{\pm i\kappa(z_{j\pm1} - z_j)} \delta_{MM'} \delta(k - k')$. The scattering matrices of each individual segment are found from the Lippmann-Schwinger equation $\Psi^{\pm} = \chi^{\pm} + G_0 v \Psi^{\pm}$

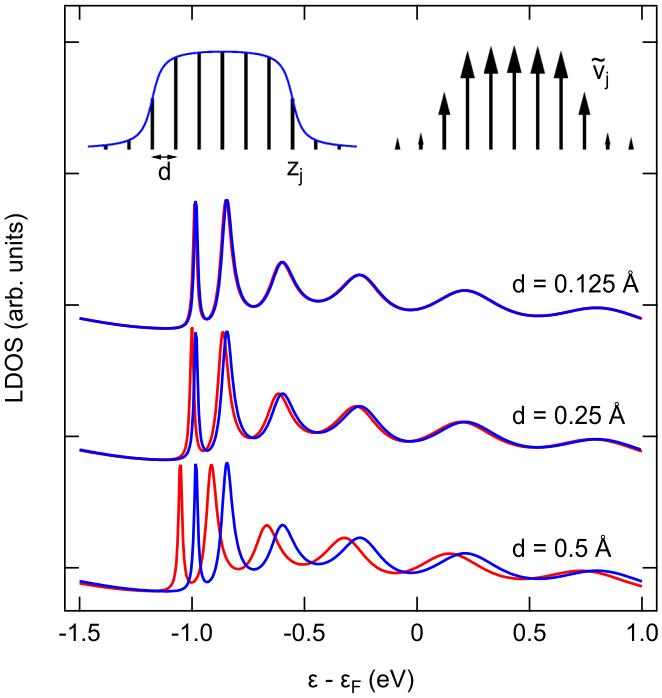

FIG. 7. Calculated LDOS above a void (cylindrical volume, height 8 Å, radius 25 Å, potential $v = 13.6$ eV, depth 11.4 Å) obtained using different δ-disk spacings d (red, vertically offset for clarity). In each case shown in blue is the LDOS obtained with $d = 0.015625$ Å. Left inset: Partitioning of void into slices, which in isolation scatter cylindrical waves. The void potential is depicted as a solid line. Right inset: Replacement of void potential by δ disks with strength $\tilde{v}_j$.

where

$$G_0(\boldsymbol{r},\boldsymbol{r}';\varepsilon) = \sum_M \int dk \chi_{Mk}(\boldsymbol{R})\chi^*_{Mk}(\boldsymbol{R}')(-i/\kappa)e^{i\kappa|z-z'|}. \tag{A4}$$

It is convenient to replace the potential v in each segment by a "δ disk" such that $v(\boldsymbol{r}) \to \tilde{v}_j(\boldsymbol{R})\delta(z - z_j)$, $|z - z_j| < d/2$, where

$$\tilde{v}_j(\boldsymbol{R}) = \int_{z_j-d/2}^{z_j+d/2} v(\boldsymbol{r})dz. \tag{A5}$$

Then formally $r_j^{-+} = r_j^{+-} = (i\kappa - \tilde{v}_j)^{-1}\tilde{v}_j$ and $t_j^{++} = t_j^{--} = 1 + r_j^{-+}$, where

$$\tilde{v}_{j,MM'}(k,k') = \int d^2\boldsymbol{R}\chi^*_{Mk}(\boldsymbol{R})\tilde{v}_j(\boldsymbol{R})\chi_{M'k'}(\boldsymbol{R}) \tag{A6}$$

and $i\kappa = i\kappa\delta_{MM'}\delta(k - k')$. This obviates the need to solve a couple-channel equation. As $d \to 0$, $\tilde{v}_j \to 0$ and it is straightforward to show that the scattering matrices given by the δ disks converge to those of the Born approximation, and correspondingly that in this limit the reflectivity $r_{1,n}^{-+}$ converges to the exact reflectivity of the void potential. Figure 7 illustrates the convergence with δ-disk thickness. Typically we use $d = 0.0625$ Å. κ becomes imaginary for $k > \sqrt{2\varepsilon}$ causing the propagators $p_j^{\pm}$ to decay exponentially, providing a natural cutoff for k integrations. Numerically, for energies close to ε_F we use 512 or 1024 regularly spaced k values extending out to $1.8\sqrt{2\varepsilon}$.

[1] S. A. Wolf, D. D. Awschalom, R. A. Buhrman, J. M. Daughton, S. von Molnár, M. L. Roukes, A. Y. Chtchelkanova, and D. M. Treger, Science **294**, 1488 (2001).

[2] G. Burkard, H.-A. Engel, and D. Loss, Spintronics, quantum computing, and quantum communication in quantum dots, in *Fundamentals of Quantum Information: Quantum Computation, Communication, Decoherence and All That*, edited by D. Heiss (Springer, Berlin, 2002), pp. 241–265.

[3] G. Konstantatos, *Colloidal Quantum Dot Optoelectronics and Photovoltaics* (Cambridge University Press, Cambridge, 2013).

[4] S. Nakamura, Rev. Mod. Phys. **87**, 1139 (2015).

[5] P. V. Kamat, J. Phys. Chem. Lett. **4**, 908 (2013).

[6] J. Zhao, M. A. Holmes, and F. E. Osterloh, ACS Nano **7**, 4316 (2013).

[7] R. E. Thomas, J. Appl. Phys. **41**, 5330 (1970).

[8] M. Milun, P. Pervan, and D. P. Woodruff, Rep. Prog. Phys. **65**, 99 (2002).

[9] J. J. Paggel, T. Miller, and T.-C. Chiang, Science **283**, 1709 (1999).

[10] X. Ma, P. Jiang, Y. Qi, J. Jia, Y. Yang, W. Duan, W.-X. Li, X. Bao, S. B. Zhang, and Q.-K. Xue, Proc. Natl. Acad. Sci. USA **104**, 9204 (2007).

[11] L. Aballe, A. Barinov, A. Locatelli, S. Heun, and M. Kiskinova, Phys. Rev. Lett. **93**, 196103 (2004).

[12] Y. Jia, M. Özer, H. Weitering, and Z. Zhang, *Nanophenomena at Surfaces: Fundamentals of Exotic Condensed Matter Properties* (Springer, Berlin, 2011), pp. 67–112.

[13] J. E. Ortega, F. J. Himpsel, G. J. Mankey, and R. F. Willis, Phys. Rev. B **47**, 1540 (1993).

[14] C. Carbone, E. Vescovo, O. Rader, W. Gudat, and W. Eberhardt, Phys. Rev. Lett. **71**, 2805 (1993).

[15] A. F. Santander-Syro, F. Fortuna, C. Bareille, T. C. Rodel, G. Landolt, N. C. Plumb, J. H. Dil, and M. Radovic, Nat. Mater. **13**, 1085 (2014).

[16] C. M. Wei and M. Y. Chou, Phys. Rev. B **66**, 233408 (2002).

[17] D. Eom, S. Qin, M.-Y. Chou, and C. K. Shih, Phys. Rev. Lett. **96**, 027005 (2006).

[18] Y. Guo, Y.-F. Zhang, X.-Y. Bao, T.-Z. Han, Z. Tang, L.-X. Zhang, W.-G. Zhu, E. G. Wang, Q. Niu, Z. Q. Qiu, J.-F. Jia, Z.-X. Zhao, and Q.-K. Xue, Science **306**, 1915 (2004).

[19] S. Qin, J. Kim, Q. Niu, and C.-K. Shih, Science **324**, 1314 (2009).

[20] A. Zhao, Q. Li, L. Chen, H. Xiang, W. Wang, S. Pan, B. Wang, X. Xiao, J. Yang, J. G. Hou, and Q. Zhu, Science **309**, 1542 (2005).

[21] T. Uchihashi, J. Zhang, J. Kröger, and R. Berndt, Phys. Rev. B **78**, 033402 (2008).

[22] R. C. Jaklevic, J. Lambe, M. Mikkor, and W. C. Vassell, Phys. Rev. Lett. **26**, 88 (1971).

[23] R. C. Jaklevic and J. Lambe, Phys. Rev. B **12**, 4146 (1975).
[24] B. J. Hinch, C. Koziol, J. P. Toennies, and G. Zhang, Europhys. Lett. **10**, 341 (1989).
[25] Y. Liu, J. J. Paggel, M. H. Upton, T. Miller, and T.-C. Chiang, Phys. Rev. B **78**, 235437 (2008).
[26] I. B. Altfeder, K. A. Matveev, and D. M. Chen, Phys. Rev. Lett. **78**, 2815 (1997).
[27] I. Vilfan, M. Henzler, O. Pfennigstorf, and H. Pfnür, Phys. Rev. B **66**, 241306 (2002).
[28] N. Miyata, K. Horikoshi, T. Hirahara, S. Hasegawa, C. M. Wei, and I. Matsuda, Phys. Rev. B **78**, 245405 (2008).
[29] P. Czoschke, H. Hong, L. Basile, and T.-C. Chiang, Phys. Rev. Lett. **91**, 226801 (2003).
[30] H. Yu, C.-S. Jiang, P. Ebert, and C.-K. Shih, Appl. Phys. Lett. **81**, 2005 (2002).
[31] Y.-F. Zhang, J.-F. Jia, T.-Z. Han, Z. Tang, Q.-T. Shen, Y. Guo, Z. Q. Qiu, and Q.-K. Xue, Phys. Rev. Lett. **95**, 096802 (2005).
[32] I.-P. Hong, C. Brun, F. Patthey, I. Y. Sklyadneva, X. Zubizarreta, R. Heid, V. M. Silkin, P. M. Echenique, K. P. Bohnen, E. V. Chulkov, and W.-D. Schneider, Phys. Rev. B **80**, 081409(R) (2009).
[33] P. S. Kirchmann, L. Rettig, X. Zubizarreta, V. M. Silkin, E. V. Chulkov, and U. Bovensiepen, Nat. Phys. **6**, 782 (2010).
[34] A. Zugarramurdi, N. Zabala, V. M. Silkin, A. G. Borisov, and E. V. Chulkov, Phys. Rev. B **80**, 115425 (2009).
[35] S. Mathias, A. Ruffing, F. Deicke, M. Wiesenmayer, M. Aeschlimann, and M. Bauer, Phys. Rev. B **81**, 155429 (2010).
[36] M. Becker and R. Berndt, Phys. Rev. B **81**, 205438 (2010).
[37] M. F. Crommie, C. P. Lutz, and D. M. Eigler, Nature (London) **363**, 524 (1993).
[38] Y. Hasegawa and P. Avouris, Phys. Rev. Lett. **71**, 1071 (1993).
[39] P. Avouris and I.-W. Lyo, Science **264**, 942 (1994).
[40] M. F. Crommie, C. P. Lutz, and D. M. Eigler, Science **262**, 218 (1993).
[41] E. J. Heller, M. F. Crommie, C. P. Lutz, and D. M. Eigler, Nature (London) **369**, 464 (1994).
[42] J. Kliewer, R. Berndt, and S. Crampin, New J. Phys. **3**, 22 (2001).
[43] J. Li, W. D. Schneider, R. Berndt, and S. Crampin, Phys. Rev. Lett. **80**, 3332 (1998).
[44] C. Tournier-Colletta, B. Kierren, Y. Fagot-Revurat, and D. Malterre, Phys. Rev. Lett. **104**, 016802 (2010).
[45] H. Jensen, J. Kröger, R. Berndt, and S. Crampin, Phys. Rev. B **71**, 155417 (2005).
[46] S. Crampin, H. Jensen, J. Kröger, L. Limot, and R. Berndt, Phys. Rev. B **72**, 035443 (2005).
[47] J. Lobo-Checa, M. Matena, K. Müller, J. H. Dil, F. Meier, L. H. Gade, T. A. Jung, and M. Stöhr, Science **325**, 300 (2009).
[48] F. Klappenberger, D. Kühne, W. Krenner, I. Silanes, A. Arnau, F. J. G de Abajo, S. Klyatskaya, M. Ruben, and J. V. Barth, Nano Lett. **9**, 3509 (2009).
[49] B. N. Taber, C. F. Gervasi, J. M. Mills, D. A. Kislitsyn, E. R. Darzi, W. G. Crowley, R. Jasti, and G. V. Nazin, J. Phys. Chem. Lett. **7**, 3073 (2016).
[50] K. Müller, M. Enache, and M. Stöhr, J. Phys.: Condens. Matter **28**, 153003 (2016).
[51] L. Bürgi, O. Jeandupeux, A. Hirstein, H. Brune, and K. Kern, Phys. Rev. Lett. **81**, 5370 (1998).
[52] A. Mugarza, A. Mascaraque, V. Pérez-Dieste, V. Repain, S. Rousset, F. J. G. de Abajo, and J. E. Ortega, Phys. Rev. Lett. **87**, 107601 (2001).
[53] A. Mugarza and J. E. Ortega, J. Phys.: Condens. Matter **15**, S3281 (2003).
[54] N. Zaki, K. Knox, P. D. Johnson, J. Fujii, I. Vobornik, G. Panaccione, and R. M. Osgood, Phys. Rev. B **83**, 205420 (2011).
[55] S. K. Hämäläinen, Z. Sun, M. P. Boneschanscher, A. Uppstu, M. Ijäs, A. Harju, D. Vanmaekelbergh, and P. Liljeroth, Phys. Rev. Lett. **107**, 236803 (2011).
[56] S.-H. Phark, J. Borme, A. L. Vanegas, M. Corbetta, D. Sander, and J. Kirschner, ACS Nano **5**, 8162 (2011).
[57] S. J. Altenburg, J. Kröger, T. O. Wehling, B. Sachs, A. I. Lichtenstein, and R. Berndt, Phys. Rev. Lett. **108**, 206805 (2012).
[58] D. Subramaniam, F. Libisch, Y. Li, C. Pauly, V. Geringer, R. Reiter, T. Mashoff, M. Liebmann, J. Burgdörfer, C. Busse, T. Michely, R. Mazzarello, M. Pratzer, and M. Morgenstern, Phys. Rev. Lett. **108**, 046801 (2012).
[59] W. Jolie, F. Craes, M. Petrović, N. Atodiresei, V. Caciuc, S. Blügel, M. Kralj, T. Michely, and C. Busse, Phys. Rev. B **89**, 155435 (2014).
[60] W. Jolie, F. Craes, and C. Busse, Phys. Rev. B **91**, 115419 (2015).
[61] N. Nilius, T. M. Wallis, and W. Ho, Science **297**, 1853 (2002).
[62] S. Fölsch, P. Hyldgaard, R. Koch, and K. H. Ploog, Phys. Rev. Lett. **92**, 056803 (2004).
[63] S. Fölsch, J. Yang, C. Nacci, and K. Kanisawa, Phys. Rev. Lett. **103**, 096104 (2009).
[64] J. Yang, C. Nacci, K. Kanisawa, and S. Fölsch, J. Vac. Sci. Technol. B **28**, C5G1 (2010).
[65] N. Néel, R. Berndt, J. Kröger, T. O. Wehling, A. I. Lichtenstein, and M. I. Katsnelson, Phys. Rev. Lett. **107**, 106804 (2011).
[66] E. H. Do and H. W. Yeom, Phys. Rev. Lett. **115**, 266803 (2015).
[67] J. Repp, P. Liljeroth, and G. Meyer, Nat. Phys. **6**, 975 (2010).
[68] S. Wang, W. Wang, and N. Lin, Phys. Rev. Lett. **106**, 206803 (2011).
[69] S. R. Schofield, P. Studer, C. F. Hirjibehedin, N. J. Curson, G. Aeppli, and D. R. Bowler, Nat. Commun. **4**, 1649 (2013).
[70] I. Swart, P. Liljeroth, and D. Vanmaekelbergh, Chem. Rev. **116**, 11181 (2016).
[71] V. Lindberg and B. Hellsing, J. Phys.: Condens. Matter **17**, S1075 (2005).
[72] W. Zhou and J. J. Coleman, Curr. Opin. Solid State Mater. Sci. **20**, 352 (2016).
[73] J. Mannhart, H. Boschker, T. Kopp, and R. Valentí, Rep. Prog. Phys. **79**, 084508 (2016).
[74] G. Reecht, H. Bulou, F. Scheurer, V. Speisser, B. Carrière, F. Mathevet, and G. Schull, Phys. Rev. Lett. **110**, 056802 (2013).
[75] Y. Zhao, J. Wyrick, F. D. Natterer, J. F. Rodriguez-Nieva, C. Lewandowski, K. Watanabe, T. Taniguchi, L. S. Levitov, N. B. Zhitenev, and J. A. Stroscio, Science **348**, 672 (2015).
[76] R. Otero, A. L. V. de Parga, and R. Miranda, Surf. Sci. **447**, 143 (2000).
[77] M. Müller, N. Néel, S. Crampin, and J. Kröger, Phys. Rev. Lett. **117**, 136803 (2016).
[78] M. Schmid, W. Hebenstreit, P. Varga, and S. Crampin, Phys. Rev. Lett. **76**, 2298 (1996).
[79] O. Kurnosikov, O. A. O. Adam, H. J. M. Swagten, W. J. M. de Jonge, and B. Koopmans, Phys. Rev. B **77**, 125429 (2008).
[80] O. Kurnosikov, D. V. Kulikov, V. S. Kharlamov, H. J. M. Swagten, and Yu. V. Trushin, Phys. Rev. B **84**, 054109 (2011).
[81] O. Kurnosikov, J. H. Nietsch, M. Sicot, H. J. M. Swagten, and B. Koopmans, Phys. Rev. Lett. **102**, 066101 (2009).

[82] O. Kurnosikov, H. J. M. Swagten, and B. Koopmans, Phys. Rev. Lett. **106**, 196803 (2011).
[83] C. Sprodowski and K. Morgenstern, Phys. Rev. B **82**, 165444 (2010).
[84] S. J. Clark, M. D. Segall, C. J. Pickard, P. J. Hasnip, M. I. J. Probert, K. Refson, and M. C. Payne, Z. Kristallogr. **220**, 567 (2005).
[85] J. P. Perdew, H. Q. Tran, and E. D. Smith, Phys. Rev. B **42**, 11627 (1990).
[86] J. R. Anderson and A. V. Gold, Phys. Rev. **139**, A1459 (1965).
[87] M. H. Upton, T. Miller, and T.-C. Chiang, Phys. Rev. B **71**, 033403 (2005).
[88] J. H. Dil, J. W. Kim, T. Kampen, K. Horn, and A. R. H. F. Ettema, Phys. Rev. B **73**, 161308 (2006).
[89] F. Yndurain and M. P. Jigato, Phys. Rev. Lett. **100**, 205501 (2008).
[90] Y. J. Sun, S. Souma, W. J. Li, T. Sato, X. G. Zhu, G. Wang, X. Chen, X. C. Ma, Q. K. Xue, J. F. Jia, T. Takahashi, and T. Sakurai, Nano Research **3**, 800 (2010).
[91] M. Hupalo and M. C. Tringides, Phys. Rev. B **65**, 115406 (2002).
[92] R. Otero, A. L. V. de Parga, and R. Miranda, Phys. Rev. B **66**, 115401 (2002).
[93] Y. Jia, B. Wu, H. H. Weitering, and Z. Zhang, Phys. Rev. B **74**, 035433 (2006).
[94] M. Becker and R. Berndt, Appl. Phys. Lett. **96**, 033112 (2010).
[95] J. Li, W.-D. Schneider, S. Crampin, and R. Berndt, Surf. Sci. **422**, 95 (1999).
[96] J. Kröger, L. Limot, H. Jensen, R. Berndt, S. Crampin, and E. Pehlke, Prog. Surf. Sci. **80**, 26 (2005).
[97] J. Kröger, M. Becker, H. Jensen, T. von Hofe, N. Néel, L. Limot, R. Berndt, S. Crampin, E. Pehlke, C. Corriol, V. Silkin, D. Sánchez-Portal, A. Arnau, E. Chulkov, and P. Echenique, Prog. Surf. Sci. **82**, 293 (2007).
[98] M. Ziegler, N. Néel, A. Sperl, J. Kröger, and R. Berndt, Phys. Rev. B **80**, 125402 (2009).
[99] J. Li, W.-D. Schneider, and R. Berndt, Phys. Rev. B **56**, 7656 (1997).